

Scalable Inference in SDEs by Direct Matching of the Fokker–Planck–Kolmogorov Equation

Arno Solin
Aalto University
Espoo, Finland
arno.solin@aalto.fi

Ella Tamir
Aalto University
Espoo, Finland
ella.tamir@aalto.fi

Prakhar Verma
Aalto University
Espoo, Finland
prakhar.verma@aalto.fi

Abstract

Simulation-based techniques such as variants of stochastic Runge–Kutta are the *de facto* approach for inference with stochastic differential equations (SDEs) in machine learning. These methods are general-purpose and used with parametric and non-parametric models, and neural SDEs. Stochastic Runge–Kutta relies on the use of sampling schemes that can be inefficient in high dimensions. We address this issue by revisiting the classical SDE literature and derive direct approximations to the (typically intractable) Fokker–Planck–Kolmogorov equation by matching moments. We show how this workflow is fast, scales to high-dimensional latent spaces, and is applicable to scarce-data applications, where a non-parametric SDE with a driving Gaussian process velocity field specifies the model.

1 Introduction

Differential equations are the standard method of modelling *change* over time. In deterministic systems the dynamics specifying how the system evolves, are typically written in the form of an ordinary differential equation (ODE). The dynamics act as prior knowledge and often stem from first-principles in application areas such as physics, control engineering, chemistry, or compartmental models in epidemiology and pharmacokinetics. Recently, learning ODE dynamics with modern automatic differentiation packages in machine learning has awakened an interest in black-box learning of continuous-time dynamics (*e.g.*, [6, 37]) and enabled their more general use across time-series modelling applications.

A stochastic differential equation (SDE, [30, 40]) can be seen as a generalization of ODEs to stochastic dynamical settings, where the driving forces fluctuate or are uncertain. Stochastic dynamics appear naturally in applications where small (and typically unobserved) forces interact with the process, such as tracking applications, molecule motion, gene modelling, or stock markets. In machine learning, SDE models have received wide-spread attention due to their robustness and appealing properties for uncertainty quantification.

The concept of a ‘solution’ to an SDE is broader than that of an ODE. As the process is stochastic, the full solution entails a probability distribution, $p(\mathbf{z}, t)$, depending on time t and covering the space \mathbf{z} (see, *e.g.*, [36]). For Itô type SDEs, the evolution of the probability mass can be described in terms of the Fokker–Planck–Kolmogorov (FPK) partial differential equation (backward Kolmogorov equation). This equation is typically intractable, and instead the *de facto* approach for inference in SDEs in machine learning is sampling. The most common approaches in this space are based on

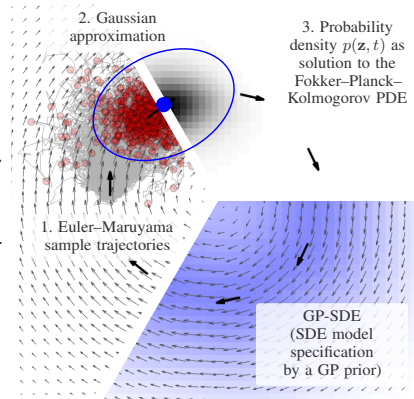


Figure 1: Views into solutions to SDEs.

Stochastic Runge–Kutta schemes (such as the *Euler–Maruyama scheme*) which are derived from the Itô–Taylor series. These schemes sample realization trajectories of the SDE by driving the dynamics with numerical simulation of Brownian motion. However, these schemes suffer from drawbacks both related to (ordinary) Runge–Kutta methods—such as step-size and sensitivity to stiffness—as well as problems associated with any sampling schemes, such as a high number of samples required for an accurate representation of the underlying distribution.

Despite these problems, few contemporary SDE approaches in machine learning explore SDE solutions beyond stochastic Runge–Kutta (or even the Euler–Maruyama scheme). Our aim is to try to broaden this view, and in Fig. 1 we sketch an example where we show three alternative solution perspectives to a Gaussian process prior SDE model (GP-SDE): the FPK probability density field, Euler–Maruyama samples, and a Gaussian assumed density approximation. We argue that a Gaussian approximation in latent space SDEs is reasonable, as Gaussian approximations are typically employed anyway in observation models, and allow for speeding-up learning by an order of magnitude.

The contributions of this paper are as follows. *(i)* We go through the workflow connecting ‘random ODE’ models with Itô SDEs driven by a Gaussian process prior over the velocity field, which allows for convenient specification of prior knowledge on the vector field and induces an implicit prior over the SDE trajectories; *(ii)* We revisit the classical SDE literature and derive direct approximations to the (typically intractable) Fokker–Planck–Kolmogorov equation in an assumed density Gaussian form that avoids sampling-based inference in the latent space, which makes inference fast and does not require sampling a high number of trajectories; *(iii)* We show how this workflow is fast, applicable to scarce-data applications, and how it also extends to previously presented latent SDE models.

1.1 Related Work

Neural ODEs [6] model ODE dynamics by a neural network. Such models were developed further in [37], where the encoder is an ODE-RNN that improves modelling of irregularly sampled time series. A latent Bayesian neural ODE model, ODE²VAE, was examined in Yıldız et al. [49], where an encoder is combined with an ODE model whose second order dynamics are given by a Bayesian neural network. The neural ODE paradigm of modelling latent dynamics has been expanded to neural SDEs [26, 12, 46, 19], where the typical workflow is that a variational autoencoder (VAE, [21, 35]) is combined with a latent neural SDE, whose drift and diffusion are modelled by neural networks. In addition to modelling time series, neural SDEs have been used in generative models [16, 43, 44], where the generation of images from noise is modelled as the reverse-time process of a diffusion SDE by using Langevin dynamics on score-based models. Continuous normalizing flows are another model family, which applies ODE dynamics in a generative model [6, 11].

These works leverage simulation/sampling for solving the SDE in the latent space. The model can be trained by a stochastic adjoint method [26, 18]. More recently, latent neural SDEs have been trained deterministically by moment matching [27]. However, they discretized the system before matching the moments, while we form a direct approximation to the solution of the FPK. Compared to optimizing the moment ODEs, as discussed in [27], by maximizing likelihood, we regularize during inference by Gaussian process priors, or prior stochastic processes as in [26]. Approximative solutions to non-linear SDEs have been applied earlier in filtering theory, where the optimal filter is approximated by a Gaussian assumed density filter [23]. In [39], such approximations are used for continuous-discrete state-space modelling. An alternative to assumed density filters are local linearization methods [31, 41], and simulation-based Itô–Taylor series solutions, stochastic Runge–Kutta methods, and leapfrog methods such as Verlet for second-order SDEs (see [22, 40]). The approximations presented in this work are also related to GP approximations [4, 2] of SDEs. The linearization approximations are related to statistical linearization [10, 42], and variational approximations [4].

Orthogonally to the SDE inference, we also consider SDE model specification in terms of GP priors. The seminal work by Rutter et al. [38] considered GP-SDE models with unit diffusion. Yıldız et al. [48] built a model, where the drift and diffusion are sparse Gaussian processes with time-independent kernels. In Hegde et al. [13], a spatio-temporal SDE with GP priors for the drift and diffusion was combined with a GP as a continuous version of deep Gaussian processes. State-space models with a GP latent state transition function [8] train a non-parametric latent process to approximate unobserved dynamics. These are related to hierarchical GP dynamics [45, 24], where prior knowledge of the system can be encoded in multi-level hierarchies, for modelling, *e.g.*, walking dynamics.

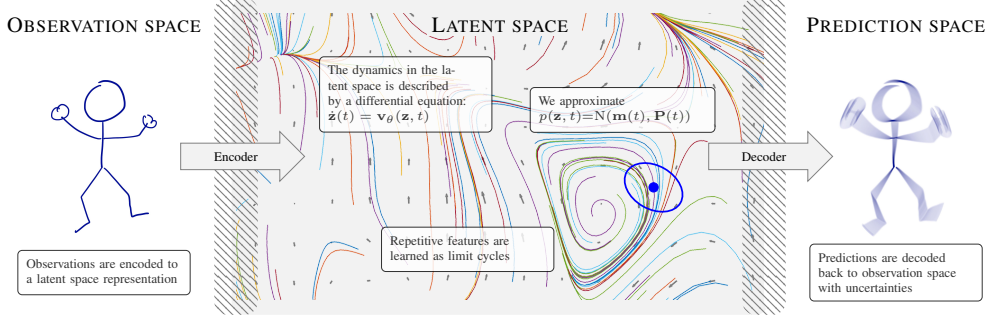


Figure 2: Latent dynamics workflow. The observations (left) are encoded into the latent space, where the dynamics of the system are learned as an SDE model. We approximate the solution to the SDE by a Gaussian for which we can approximate the dynamics of the first moments by an ODE system, thus avoiding sampling in the latent space. Predictions are finally mapped back.

2 Methods

We draft the methodology based on the latent dynamics workflow components as presented in Fig. 2. The focus is first on specifying models for the latent space dynamics, starting from implicit priors in terms of random ODEs which we frame as Itô SDEs. Thereafter, the focus shifts from model specification to inference, where we show that the Fokker–Planck–Kolmogorov equation can be efficiently approximated in an assumed density form, and finally brings us to cover the likelihood structure of these models as well.

2.1 Random Field Ordinary Differential Equations as SDEs

The continuous dynamics of a latent (unobserved) $\mathbf{z}(t) \in \mathbb{R}^d$ can conveniently be written in the form of a general first-order ordinary differential equation

$$\frac{d}{dt}\mathbf{z}(t) = \mathbf{v}_\theta(\mathbf{z}(t), t), \quad (1)$$

where $\mathbf{v}_\theta(\cdot) : \mathbb{R}^d \times \mathbb{R}_+ \rightarrow \mathbb{R}^d$ denotes the velocity field parametrized by θ . This is a general form of a non-linear ODE system, where the dynamics are deterministic and fully characterized by $\mathbf{v}_\theta(\cdot)$. The methodology presented in this section directly extends to the case where the vector field \mathbf{v}_θ is time-dependent, but we omit the time dimension for simplicity of notation. Previously, the implicit prior on $\mathbf{z}(t)$ over t specified by Eq. (1) has been generalized to stochastic models by considering $\mathbf{v}_\theta(\cdot)$ to be stochastic. These models are known as ‘random’ ODE models, and the random field $\mathbf{v}_\theta(\cdot)$ is typically either characterized by a Gaussian random field or Gaussian process model (see, *e.g.*, [38, 13]) or some parametric model (*e.g.*, [26]).

We consider an unconventional ODE model (or actually no ODE model at all, to be precise), where we specify a GP prior [34] over the velocity field in form of a multi-output Gaussian process prior:

$$\mathbf{v}(\mathbf{z}, t) \sim \text{GP}(\boldsymbol{\mu}(\mathbf{z}), \boldsymbol{\kappa}(\mathbf{z}, \mathbf{z}')), \quad (2)$$

where $\boldsymbol{\mu} : \mathbb{R}^d \rightarrow \mathbb{R}^d$ is a mean function and $\boldsymbol{\kappa} : \mathbb{R}^d \times \mathbb{R}^d \rightarrow \mathbb{R}^{d \times d}$ is a matrix-valued covariance function. The Gaussian process prior is completely specified by its mean and covariance function, which encapsulate the assumptions about the sample processes/fields \mathbf{v} (such as continuity, differentiability, curl, divergence, *etc.*): $\boldsymbol{\mu}(\mathbf{z}) := \mathbb{E}[\mathbf{v}(\mathbf{z})]$ and $\boldsymbol{\kappa}(\mathbf{z}, \mathbf{z}') := \mathbb{E}[(\mathbf{v}(\mathbf{z}) - \boldsymbol{\mu}(\mathbf{z}))(\mathbf{v}(\mathbf{z}') - \boldsymbol{\mu}(\mathbf{z}'))^*]$. In Fig. 3, we will consider examples of useful vector-valued covariance functions that encode properties on the vector field. For inference, the GP is conditioned on input–output pair observations $\mathcal{D} = \{(\mathbf{z}_i, \Delta\mathbf{z}_i)\}_{i=1}^n$ of the vector field, where $\Delta\mathbf{z}_i$ represents the observed derivative at \mathbf{z}_i . The conditioned vector field representation for an arbitrary point \mathbf{z}_* in the latent space can be given by

$$\mathbf{v}(\mathbf{z}_*) | \mathcal{D} \sim \text{GP}(\mathbb{E}[\mathbf{v}(\mathbf{z}) | \mathcal{D}], \text{Cov}[\mathbf{v}(\mathbf{z}) | \mathcal{D}]), \quad (3)$$

where the $\mathbb{E}[\cdot]$ and $\text{Cov}[\cdot]$ denote the marginal mean and (co)variance (for the multi-output GP, which means that the marginals are vector-valued). These take the form [34]: $\mathbb{E}[\mathbf{v}(\mathbf{z}_*)] = \mathbf{K}_* \hat{\mathbf{K}}^{-1} \mathbf{y}$ and

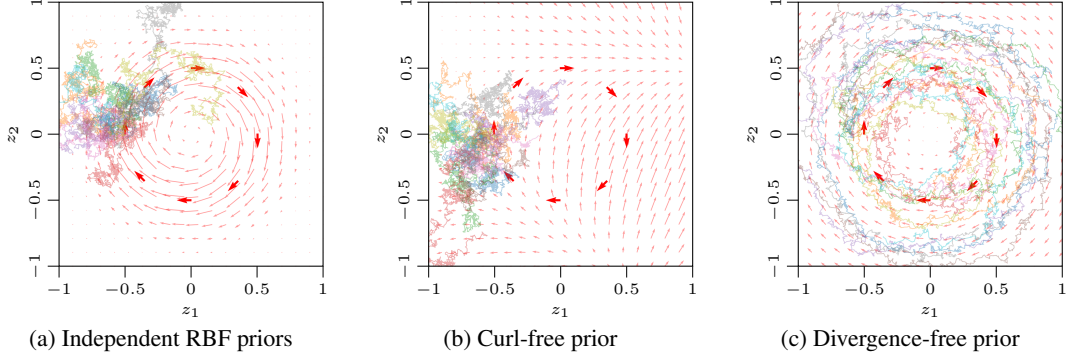


Figure 3: Effect of different GP priors in an GP-SDE with 8 observations (large red arrows) to the GP posterior (small red arrows): (a) Shows results for independent RBF priors over z_1 and z_2 ; (b) shows results for the curl-free covariance function (encoding ‘loop-aversion’); (c) shows results for the divergence-free covariance function (encoding ‘energy preservation’). The hyperparameters ($\ell = 0.2, \sigma^2 = 0.1$) are the same in each.

$\text{Cov}[\mathbf{v}(\mathbf{z}_*)] = \kappa(\mathbf{z}_*, \mathbf{z}_*) - \mathbf{K}_* \hat{\mathbf{K}}^{-1} \mathbf{K}_*^\top$, where \mathbf{y} are the stacked observations of the derivatives such that $\mathbf{y} = (\Delta \mathbf{z}_1^\top, \dots, \Delta \mathbf{z}_n^\top)^\top$. The Gram matrix \mathbf{K} corresponds to evaluations of the covariance function such that $\mathbf{K}_{ij} = \kappa(\mathbf{z}_i, \mathbf{z}_j)$ are sub-blocks of \mathbf{K} corresponding to the observation pairs (i, j) , and $\hat{\mathbf{K}} = \mathbf{K} + \gamma \mathbf{I}$, where γ is a nugget (observation noise/discrepancy) term, and \mathbf{K}_* is the cross-covariance between \mathbf{z} and \mathbf{z}_* . The prohibitive cubic computational scaling associated with GP models manifests in the inversion of $\hat{\mathbf{K}}$, and thus for large n , approximations based on inducing points or projections are used in practice to avoid this explicit inversion. In the light of Eq. (1) with $\mathbf{v}(\mathbf{z}) \sim \text{GP}(\cdot, \cdot)$, the ODE is driven by a multi-dimensional Gaussian random field conditioned on \mathcal{D} . A straightforward way of dealing with a model of this kind, is to do inference by sampling random draws of the velocity field from the GP, and then drive the ODE with those samples (can be viewed as an Monte Carlo approach for drawing ODE realizations).

However, a more convenient way is to specify the prior over the stochastic dynamics in a stochastic differential equation form. At its core, a lot of previous work in this space hinges on the realization that if everything is essentially Gaussian, an equivalent model can be specified in terms of an Itô SDE describing the stochastic evolution of trajectories affected by the GP velocity field [see 13, for discussion]. Informally, this takes the white noise form $\frac{d}{dt} \mathbf{z}(t) = \mathbf{f}(\mathbf{z}) + \mathbf{L}(\mathbf{z}) \mathbf{w}(t)$, where $\mathbf{f}(\mathbf{z}) = \mathbb{E}[\mathbf{v}(\mathbf{z})]$ and $\mathbf{L}(\mathbf{z})$ denotes a square-root factor such that $\mathbf{L} \mathbf{L}^\top = \text{Cov}[\mathbf{v}(\mathbf{z})]$ (in the scalar case, just the square-root, and in the multi-output case, *e.g.*, the Cholesky factor). Here $\mathbf{w}(t)$ is a white noise process with unit spectral density. It is worth noting that we do not give guarantees for a direct link between the random ODE in Eq. (2) and the following SDE formulation (see App. A.3 for discussion). Yet, formally we write a similarly-behaving SDE in the standard Itô SDE form:

$$d\mathbf{z}(t) = \mathbf{f}(\mathbf{z}, t) dt + \mathbf{L}(\mathbf{z}, t) d\beta(t), \quad (4)$$

where $d\beta(t)$ is vector-valued unit Brownian motion (the spectral density \mathbf{Q} is set to \mathbf{I}). For a GP-SDE, the drift is driven by the GP mean, $\mathbf{f}(\mathbf{z}, t) := \mathbb{E}[\mathbf{v}(\mathbf{z})]$ and the diffusion by the square-root factor of the marginal covariance at $\mathbf{z}(t)$, $\mathbf{L}(\mathbf{z}, t) := \sqrt{\text{Cov}[\mathbf{v}(\mathbf{z})]}$. To be precise, the GP-SDE drift and diffusion at a point \mathbf{z}_* are determined by the GP predicted mean and variance at \mathbf{z}_* , which can be written as

$$\mathbf{f}(\mathbf{z}_*, t) = \mathbb{E}[\mathbf{v}(\mathbf{z}_*)] = \mathbf{K}_* \hat{\mathbf{K}}^{-1} \mathbf{y} \quad \text{and} \quad \mathbf{L}(\mathbf{z}_*, t) = \sqrt{\text{Cov}[\mathbf{v}(\mathbf{z}_*)]} = \sqrt{\kappa(\mathbf{z}_*, \mathbf{z}_*) - \mathbf{K}_* \hat{\mathbf{K}}^{-1} \mathbf{K}_*^\top}. \quad (5)$$

2.2 Fokker–Planck–Kolmogorov Equation

We are interested in *solving* SDE models of the form in Eq. (4), but without the restriction that the drift and diffusion are defined by a Gaussian process, and present the related theory with a model-agnostic view on the problem. Because the resulting solutions are stochastic processes, the full solution to the SDE can be characterized by its time-evolving probability density function. Let $\mathbf{z}(t_0) \sim p(\mathbf{z}(t_0))$ be some initial condition which we assumed to be independent of the Brownian motion. The probability

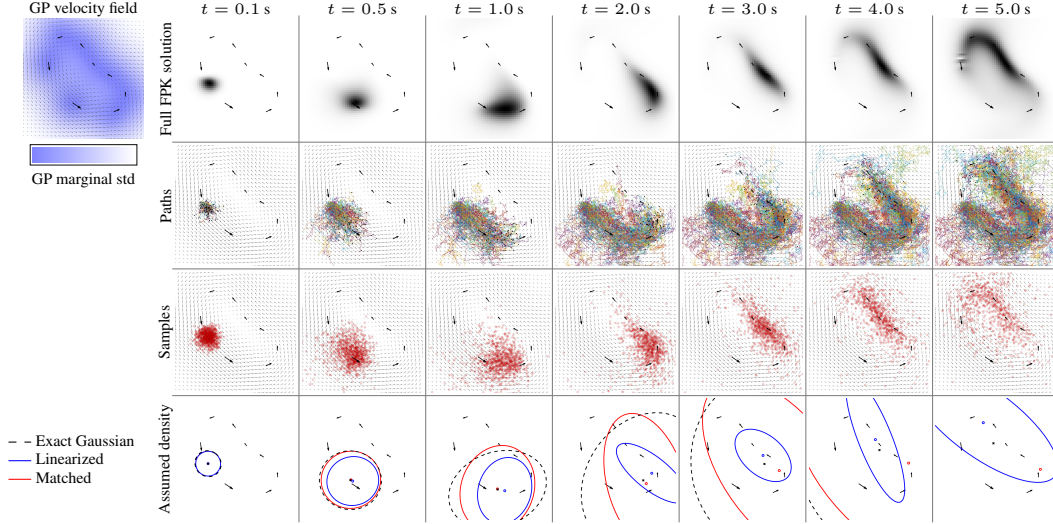


Figure 4: Approximations to the FPK equation: The **top-left** figure shows the 8 observations (black arrows) and the inferred GP velocity (grey arrows, marginal uncertainty in shaded blue). The **top-row** shows the progression of the probability mass $p(\mathbf{z}, t)$ following the Fokker–Planck–Kolmogorov equation. The **middle rows** show Euler–Maruyama sample trajectories for the problem, and the **bottom row** compares the two assumed density approximations to the exact Gaussian approximation of the FPK solution. The bottom row ellipses are 95% confidence regions.

density $p(\mathbf{z}, t)$ of the solution of the SDE in Eq. (4) solves the Fokker–Planck–Kolmogorov (FPK) partial differential equation (PDE):

$$\frac{\partial p(\mathbf{z}, t)}{\partial t} = - \sum_i \frac{\partial}{\partial z_i} [f_i(\mathbf{z}, t) p(\mathbf{z}, t)] + \frac{1}{2} \sum_{i,j} \frac{\partial^2}{\partial z_i \partial z_j} \{ [\mathbf{L}(\mathbf{z}, t) \mathbf{Q} \mathbf{L}^\top(\mathbf{z}, t)]_{ij} p(\mathbf{z}, t) \}. \quad (6)$$

For a proof, see [40]. This PDE is also known as the Fokker–Planck equation (in physics) and the forward Kolmogorov equation (in stochastic). An appealing alternative form [40, Sec. 5.3] of the FPK equation can be given in terms of the following evolution equation with the adjoint operator \mathcal{A}^* :

$$\frac{\partial p}{\partial t} = \mathcal{A}^* p, \text{ with } \mathcal{A}^*(\bullet) = - \sum_i \frac{\partial}{\partial z_i} [f_i(\mathbf{z}, t) (\bullet)] + \frac{1}{2} \sum_{i,j} \frac{\partial^2}{\partial z_i \partial z_j} \{ [\mathbf{L}(\mathbf{z}, t) \mathbf{Q} \mathbf{L}^\top(\mathbf{z}, t)]_{ij} (\bullet) \}. \quad (7)$$

Eq. (7) allows for various kind of approaches for direct approximation of the FPK equation either by basis function approximations, finite differences, or other methods (Sec. 9.6 in [40] provides examples of using point collocation, Ritz–Galerkin, and FEM type of methods for approximating the solution). For example, the results in Fig. 1 and Fig. 4 are estimated by a grid discretization over \mathbf{z} and solving the resulting (finite-dimensional) ODE corresponding to Eq. (7) by the matrix exponential: $\mathbf{p}(t) = \exp(\mathbf{A}(t - t_0))$. See App. A.2 for details. Even if the widely-used Euler–Maruyama, Milstein, and more general stochastic Runge–Kutta schemes are derived from the Itô–Taylor series, the resulting methods can still be viewed as an approximation of $p(\mathbf{z}, t)$.

2.3 Assumed Density Approximation of FPK

For the purpose of modelling latent space dynamics of systems of the kind in Fig. 2, we note that there the common practice of solving the latent SDE through costly simulation/sampling and then employing a variational (Gaussian) approximation in the encoder/decoder seems contradictory. That is, it might be unnecessary to sample realizations of the trajectory dynamics, if the interest is only in the time-marginals of the process. Thus, we seek to directly characterize the first two moments of the solution to the FPK equation in Sec. 2.2. We replace the FPK solution with a Gaussian approximation of form

$$p(\mathbf{z}, t) \approx \mathcal{N}(\mathbf{z} | \mathbf{m}(t), \mathbf{P}(t)), \quad (8)$$

where $\mathbf{m}(t)$ and $\mathbf{P}(t)$ are interpreted as a mean and covariance of the state of the solution at time t . This kind of approximation is commonly referred to as a Gaussian *assumed density* approximation (see, e.g., [23, 39]), because the computations are done under the assumption that the state distribution is Gaussian. Assumed density approximations are common in signal processing–driven SDE methodology, and we refer the reader to Sec. 9.1 in [40] for a detailed overview. Following [39], we revisit the idea that a Gaussian process approximation to the SDE Eq. (4) can be obtained by integrating the following differential equations from the initial conditions $\mathbf{m}(t_0) = \mathbb{E}[\mathbf{z}(t_0)]$ and $\mathbf{P}(t_0) = \text{Cov}[\mathbf{z}(t_0)]$ to the target time t :

$$\frac{d\mathbf{m}}{dt} = \int \mathbf{f}(\mathbf{z}, t) N(\mathbf{z} | \mathbf{m}, \mathbf{P}) d\mathbf{z} \quad \text{and} \quad (9)$$

$$\begin{aligned} \frac{d\mathbf{P}}{dt} = & \int \mathbf{f}(\mathbf{z}, t) (\mathbf{z} - \mathbf{m})^\top N(\mathbf{z} | \mathbf{m}, \mathbf{P}) d\mathbf{z} \\ & + \int (\mathbf{z} - \mathbf{m}) \mathbf{f}^\top(\mathbf{z}, t) N(\mathbf{z} | \mathbf{m}, \mathbf{P}) d\mathbf{z} + \int \mathbf{L}(\mathbf{z}, t) \mathbf{Q} \mathbf{L}^\top(\mathbf{z}, t) N(\mathbf{z} | \mathbf{m}, \mathbf{P}) d\mathbf{z}. \end{aligned} \quad (10)$$

These equations for the evolution of the first moments of the solution to the SDE can be interpreted as expectations over the drift and diffusion dynamics of the SDE, and can be derived from the FPK in Eq. (6). Conveniently, these expressions are *not* stochastic, but instead take the form of an ODE system that—given the integrals are tractable—can be solved with out-of-the-box ODE solvers. However, even if Eqs. (9) and (10) provide a generic Gaussian assumed density approximation framework for SDEs, an implementation of the method requires solving the following kind of d -dimensional Gaussian integrals:

$$\mathbb{E}_N[\bullet] = \int [\bullet] N(\mathbf{z} | \mathbf{m}, \mathbf{P}) d\mathbf{z}. \quad (11)$$

In the following sections we will consider two approaches (local linearization and moment matching with symmetric quadrature) which scale linearly in the number of latent dimensions d .

2.4 Linearizing the FPK Equation

Local linearization around the \mathbf{m} (via a Taylor series approximation) is a classical approach widely used for this type of Gaussian integrals in machine learning and filtering theory [17, 29]. If the function $\mathbf{f}(\mathbf{z}, t)$ is differentiable, the covariance differential equation can be simplified by using Stein’s lemma [32] such that

$$\int \mathbf{f}(\mathbf{z}, t) (\mathbf{z} - \mathbf{m})^\top N(\mathbf{z} | \mathbf{m}, \mathbf{P}) d\mathbf{z} = \left[\int \mathbf{F}_z(\mathbf{z}, t) N(\mathbf{z} | \mathbf{m}, \mathbf{P}) d\mathbf{z} \right] \mathbf{P}, \quad (12)$$

where $\mathbf{F}_z(\mathbf{z}, t)$ is the Jacobian of $\mathbf{f}(\mathbf{z}, t)$ with respect to \mathbf{z} . Linearizing around the mean \mathbf{m} and approximating the diffusion as $\mathbf{L}(\mathbf{z}, t) \approx \mathbf{L}(\mathbf{m}, t)$ gives a linearized form of Eqs. (9) and (10):

$$\frac{d\mathbf{m}}{dt} = \mathbf{f}(\mathbf{m}, t) \quad \text{and} \quad \frac{d\mathbf{P}}{dt} = \mathbf{P} \mathbf{F}_z^\top(\mathbf{m}, t) + \mathbf{F}_z(\mathbf{m}, t) \mathbf{P} + \mathbf{L}(\mathbf{m}, t) \mathbf{Q} \mathbf{L}^\top(\mathbf{m}, t), \quad (13)$$

which provides a direct way of propagating the moments of the latent SDE through an ODE for the mean and covariance without the need of drawing multiple sample trajectories. The resulting ODE is $(d + d^2)$ -dimensional, and only requires one evaluation of the drift, diffusion, and Jacobian per step.

2.5 Matching Moments of the FPK Equation

The local linearization approach given in the preceding section is efficient, but fully *local*. An alternative way of constructing an assumed density approximation to $p(\mathbf{z}, t)$ is to directly match the moments by solving the Gaussian integrals in Eqs. (9) and (10) by Gaussian quadrature methods. The approximation to Eq. (11) would take the form $\int \mathbf{g}(\mathbf{z}, t) N(\mathbf{z} | \mathbf{m}, \mathbf{P}) d\mathbf{z} \approx \sum_i w^{(i)} \mathbf{g}(\mathbf{z}^{(i)}, t)$, for an arbitrary integrand $\mathbf{g}(\mathbf{z}, t)$, weights $w^{(i)}$, and so called sigma points $\mathbf{z}^{(i)} = \mathbf{m} + \sqrt{\mathbf{P}} \boldsymbol{\xi}_i$. Here $\sqrt{\mathbf{P}}$ denotes a square-root factor of \mathbf{P} such as the Cholesky decomposition. The multi-dimensional Gaussian quadrature (or *cubature*, see [7]) rule is characterized by the evaluation points and their associated weights $\{(\boldsymbol{\xi}_i, w_i)\}$. We write Eqs. (9) and (10) in a Gaussian assumed density form which matches the moments by quadrature as follows [40]:

$$\frac{d\mathbf{m}}{dt} = \sum_i w^{(i)} \mathbf{f}(\mathbf{m} + \sqrt{\mathbf{P}} \boldsymbol{\xi}_i, t) \quad \text{and} \quad (14)$$

$$\begin{aligned} \frac{d\mathbf{P}}{dt} = & \sum_i w^{(i)} \mathbf{f}(\mathbf{m} + \sqrt{\mathbf{P}} \boldsymbol{\xi}_i, t) \boldsymbol{\xi}_i^\top \sqrt{\mathbf{P}}^\top \\ & + \sum_i w^{(i)} \sqrt{\mathbf{P}} \boldsymbol{\xi}_i \mathbf{f}^\top(\mathbf{m} + \sqrt{\mathbf{P}} \boldsymbol{\xi}_i, t) + \sum_i w^{(i)} \mathbf{L}(\mathbf{m} + \sqrt{\mathbf{P}} \boldsymbol{\xi}_i, t) \mathbf{Q} \mathbf{L}^\top(\mathbf{m} + \sqrt{\mathbf{P}} \boldsymbol{\xi}_i, t). \end{aligned} \quad (15)$$

The computational complexity of this approach is highly dependent on the choice of quadrature method. A typical choice in ML applications would be Gauss–Hermite quadrature, which factorizes over the input dimensions leading to an exponential number (p^d) of function evaluations/sigma points in the input dimensionality d for a desired order p . In order to guarantee scalability, we employ a symmetric 3rd order cubature rule [3] which similarly to Gauss–Hermite ($p = 3$) is exact for polynomials up to degree 3. The points are given by scaled unit coordinate vectors \mathbf{e}_i such that

$$\xi_i = \begin{cases} \sqrt{d}\mathbf{e}_i, & \text{for } i = 1, \dots, d, \\ -\sqrt{d}\mathbf{e}_i, & \text{for } i = d + 1, \dots, 2d, \end{cases} \quad (16)$$

and the associated weights are $w_i = \frac{1}{2d}$. This approach provides a direct way of propagating the ‘true’ moments of the latent SDE through an ODE for the mean and covariance and without the need of drawing multiple sample trajectories. The resulting ODE is $(d + d^2)$ -dimensional, and requires only $2d$ evaluations of the drift and diffusion per step.

2.6 Analysis of the Computational Complexity

In terms of the asymptotic computational complexity, the linearization approach in Sec. 2.4 requires $\mathcal{O}(1)$ evaluations of the drift, diffusion, and Jacobian per step. The moment matching approach in Sec. 2.5 requires $\mathcal{O}(d)$ evaluations of the drift and diffusion as well as an $\mathcal{O}(d^3)$ Cholesky decomposition per step. The simplest Monte Carlo simulation method with p samples requires $\mathcal{O}(p)$ evaluations of the drift and diffusion per step. Additionally, the naïve requirement for p grows exponentially in d . On the other hand, the simulation approach is fully parallelizable over p , while the moment matching approach the number of nonparallelizable operations is $\mathcal{O}(d^2)$ with the Cholesky decomposition being the bottleneck, and the linearization approach is nonparallelizable. While the linearization approach has the lowest number of function evaluations with respect to d , the cost of computing the Jacobian can be prohibitively large for arbitrarily complex models. Nevertheless, the Jacobian is available in closed-form for GPs and may be evaluated reasonably fast for neural network based drifts, see App. B.2 for empirical computational costs of evaluating the Jacobian when growing the network size. Thus we expect the FPK approximation schemes to always be beneficial in CPU-only cases (incl. CPU multi-threading and embedded devices). In multicore GPU use, for low-dimensional d , sampling remains appealing if GPU memory does not become a bottleneck.

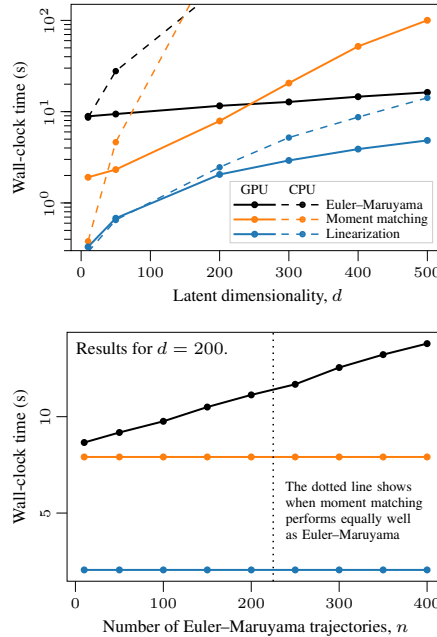
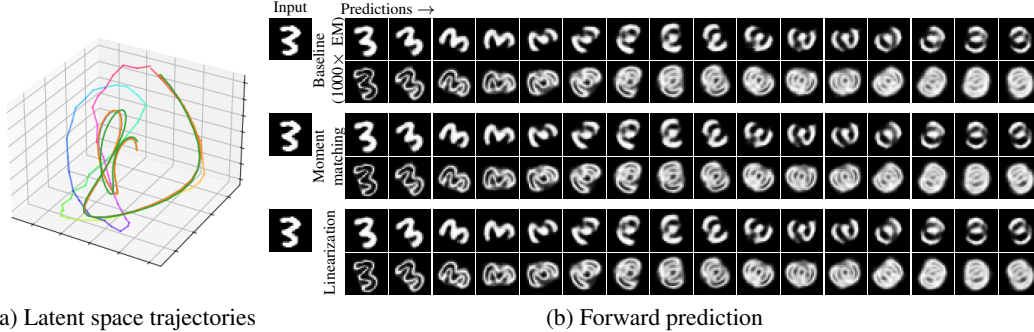


Figure 5: Empirical timing experiments with error of final margins matched.

3 Experiments

The goals of the experiments are three-fold: We first provide a study of the computational complexity. Then, we look into properties of the GP-SDE model from Sec. 2.1, where the experiments are concerned with showcasing model specification rather than inference. Finally, we consider two benchmark problems with high-dimensional inputs for learning a latent SDE model, where we test the performance of the approximations presented when the model is not defined by GPs, as the SDE methods presented in Sec. 2 are model-agnostic.

Timing Experiments To confirm the analysis in Sec. 2.6 and provide a practical insight, we run numerical experiments with the error of final marginal mean/covariance controlled. We use a high-dimensional model of d independent Beneš SDEs ($dz(t) = \tanh(z) dt + d\beta(t)$, see [40]) with different z_0 per dimension. The model is non-linear and solution-space multi-modal, but both $p(\mathbf{z}, t)$ and the marginal moments $(\mathbf{m}(t), \mathbf{P}(t))$ are available in closed form (see App. B.1). In comparison



(a) Latent space trajectories (b) Forward prediction

Figure 6: Results on rotating MNIST. (a) shows the latent space prediction mean trajectories for one test image. Evolution of the true trajectory is shown in HSV colour and the predicted trajectory by Euler–Maruyama, moment matching, and linearization scheme is shown in green, blue, and orange (all overlapping one another). (b) shows the progression of the prediction (mean and std dev) of the test image, when it traverses the learned dynamics in the latent space. Both the moment matching and linearization schemes match the baseline (with 1000 Euler–Maruyama trajectories).

to Euler–Maruyama, we control the number of trajectories n by bounding the error (in terms of KL divergence) between Euler–Maruyama and the ground-truth to match the error in our moment matching approach, and consider the methods equivalent in terms of the quality of the solution. See App. B.1 for the required number of trajectories to match the KL divergence for each dimensionality plotted. Fig. 5 shows GPU/CPU wall-clock times (GPU: NVIDIA Tesla V100 32 GB with Intel Xeon Gold 6134 3.2 GHz; CPU: Xeon Gold 6248 2.50GHz). We implement the models in PyTorch [33] and report means of 10 repetitions (std negligible). In low-dimensional cases, both approximation methods outperform sampling, whereas in high dimensions GPU parallelisation becomes dominant and only the linearized approximation remains highly competitive. This example should favour sampling: In the Beneš model, the number of trajectories, n , per d in Euler–Maruyama remains low (n is linear in d), which is due to the diagonal (independent) diffusion matrix. In a correlated latent space n would grow super-linearly (even exponentially), which would further push the difference between methods.

GP-SDE Model Specification We consider an GP-SDE model with just 8 observations of the dynamics, where the lack of data can be compensated for with encoding prior knowledge into the model. We use the model formulation given in Sec. 2.1, and study the effect of GP priors, the first of which is an independent squared exponential (RBF) prior for each dimension which encode continuity and smoothness in the velocity field. The second GP prior is the multi-dimensional curl-free kernel [47] (see App. B.3) which encodes the assumption of a curl-free random vector field. This property can be interpreted as ‘loop aversion’ in the GP-SDE context. The third prior, is a multi-dimensional divergence-free kernel [47] which encodes the assumption of no divergence in the random vector field. This property can be interpreted as ‘energy preservation’ or source-freeness. These properties are visible in Fig. 3, where the hyperparameters are fixed to same values for all models.

Assumed Density Approximation of the FPK We provide an illustrative example of the moment evolution methods in a GP-SDE model with 8 observations along a bean curve and independent squared exponential GP priors per dimension. As a baseline, we solve the FPK in Eq. (7) by finite-differences discretization in \mathbf{z} (see App. A.2 for details). Fig. 4 shows the evolution of the SDE solution over the time-course of 5 s. The probability mass dissolves quickly, which is hard to interpret from the top-row figure alone. Comparison between the point clouds and the top row shows that even with 1000 trajectories and just a two-dimensional space, it is hard to capture detailed structure in the SDE solution. The bottom row compares the local linearization (Sec. 2.4) and the moment matching (Sec. 2.5) assumed density approximations to the exact Gaussian approximation of the FPK solution. The linearized approach is mode-seeking (matches local curvature), while the moment matching approach captures the overall structure of the optimal Gaussian approximation.

Rotating MNIST In the spirit of Fig. 2, we run the proposed methods on Rotating MNIST ([25], available under CC BY-SA 3.0), similar to [49, 5]. The data set consists of various handwritten digit ‘3’s rotated uniformly in 64 angles. We train a VAE [21] first by freezing the latent space dynamics, allowing us to generate the latent samples for learning the dynamics by applying the

Table 1: Rotating MNIST results.

INFERENCE SCHEME	MSE	NLPD ($t = 64$)
Euler–Maruyama	0.046 ± 0.006	33.0 ± 5.4
Moment matching	0.051 ± 0.007	52.7 ± 9.5
Linearization	0.052 ± 0.007	54.5 ± 9.9

Table 2: Wall-clock timings for MOCAP.

TIME/S \pm STD	NUMBER OF E-M PATHS				
	LIN.	MOM. MAT.	1	25	200
GPU 2.1 ± 1	6.0 ± 1	37.1 ± 1	39.9 ± 1	40.4 ± 7	
CPU 1.8 ± 1	1.8 ± 1	27.7 ± 7	38.6 ± 1.5	94.2 ± 3.5	

Table 3: Test MSE on 297 future MOCAP points averaged over 50 samples. 95% confidence interval reported based on t-statistic. [†]results from [49], [‡]results from [26]

METHOD	TEST MSE
DTSBN-S [9]	$34.86 \pm 0.02^{\dagger}$
npODE [14]	22.96^{\dagger}
NeuralODE [6]	$22.49 \pm 0.88^{\dagger}$
ODE ² VAE [49]	$10.06 \pm 1.4^{\dagger}$
ODE ² VAE-KL [49]	$8.09 \pm 1.95^{\dagger}$
Latent ODE [37]	$5.98 \pm 0.28^{\ddagger}$
Latent SDE [26]	$4.03 \pm 0.20^{\ddagger}$
Latent SDE (assumed density)	7.55 ± 0.05

trained VAE. Then freezing the VAE encoder/decoder and training a 16-dimensional GP-SDE model in the latent space with independent squared exponential GP priors (see App. B.5). In Fig. 6 we feed in one observation and let it follow the learned dynamics of rotation. As the baseline, we use 1000 trajectories computed using Euler–Maruyama. Fig. 6a demonstrates the model’s capability to learn the latent trajectory, and we show the trajectories for all the methods in three latent dimensions with most variation. The trajectories for the three methods overlap, and qualitatively the results are identical in Fig. 6b. Quantitatively the brute-force sampling baseline gives slightly better MSEs over images and final-step mean negative log predictive densities (NLPD, see Table 1).

Motion Capture Data The CMU walking data set ([1], CMU MoCap available under CC BY-ND 4.0) is a real-world noisy data set with 50 sensors that track a human subject’s walking. As in Yıldız et al. [49] and Li et al. [26], we model the sequences of a single subject, 35, for which there are 16 train set, three validation set and four test set sequences. The task is to predict the state of the system in the future given three initial points. In this experiment, we demonstrate that replacing SDE solver-based methods by an assumed density approximation, a latent neural SDE system can be learned efficiently without sampling trajectories. For this purpose, and for better comparability to earlier work, the latent SDE drift and diffusion are neural networks. As in Li et al. [26], we regularize the learned posterior process by a prior process. The loss function consists of three terms: reconstruction loss, VAE encoded initial position KL-divergence, and the KL-divergence between posterior/prior processes. The moments of the posterior SDE approximation are denoted by $\mathbf{m}(t)$, $\mathbf{P}(t)$, those of the prior process $\mathbf{m}_*(t)$, $\mathbf{P}_*(t)$, and the observation times by $\{t_j\}_{j=0}^m$. The loss becomes

$$\begin{aligned} \mathcal{L} = & - \sum_{j=0}^m \log p(\mathbf{x}(t_j) | \mathbf{z}(t_j)) + D_{\text{KL}} [q(\mathbf{z}(t_0) | \mathbf{x}(t_0)) \| p(\mathbf{z})] \\ & + \sum_{j=1}^m \gamma D_{\text{KL}} [N(\mathbf{m}(t_j), \mathbf{P}(t_j)) \| N(\mathbf{m}_*(t_j), \mathbf{P}_*(t_j))], \quad (17) \end{aligned}$$

where $\mathbf{z}(t_j)$ and $\mathbf{x}(t_j)$ are the latent codes and observations, respectively, q denotes the conditional encoder distribution, $p(z)$ is the normal distribution, and $\log p(\mathbf{x}(t_j) | \mathbf{z}(t_j))$ is the model likelihood of the observations, given latent codes. While training, the parameters to optimize include those of a latent neural network which defines the prior and posterior dynamics, and of the VAE which encodes an initial point and decodes at each discrete time step corresponding to a train set frame. As the VAE is trained simultaneously to the latent dynamics, the approach does not provide a set of true latent samples to compare to, in contrast to the MNIST experiments. The VAE encoder prior is the normal distribution, whereas the encoder posterior is acting as the initial distribution for the latent SDEs. For the encoder design, we use a fully-connected neural network, which encodes the three first data points to create latent state and context vectors. As the prior process was a SDE with zero drift and $\sigma \mathbf{I}$ diffusion. The context is passed through the dynamics, similar to the treatment of velocity in Yıldız et al. [49] (see App. B.6).

The result in Table 3 is competitive considering that solving the latent SDE with the linearization approach roughly matches the required computation budget for *one* stochastic Runge–Kutta sample in the other methods. This is highlighted in Table 2 which shows the wall-clock times for the model used in this experiment both in a CPU and a GPU setting (see hardware description in previous experiment).

4 Discussion and Conclusions

In this paper our interest has been in both SDE model specification and approximative inference. We considered GP-SDE models for data-scarce applications that need injection of prior knowledge such as in Fig. 3. For inference, we built upon the established methodology of assumed density approximations in signal processing for directly approximating the solution distribution of an Itô SDE, where the methods apply to any latent space SDE models.

We put interest in *weak* solution concepts for SDEs. We considered both linearization and moment matching based methods for capturing the first two moments of the SDE solutions, which respectively require only $\mathcal{O}(1)$ and $\mathcal{O}(d)$ evaluations of the model functions per solver step in latent space dimensionality d . Furthermore, they only require solving of one ODE rather than simulating multiple trajectories. This makes them orders of magnitudes lighter than the current state-of-the-art in neural SDEs, which we analyzed both through theoretical bounds in Sec. 2.6, ran numerical experiments with the final error controlled (Fig. 5), and highlighted the practical wall-clock time in a MOCAP experiment. We further argued that a Gaussian assumption makes sense in applications of the form in Fig. 2 as one is typically employed anyway in the encoder–decoder.

There are some key differences between our assumed density approach and commonly used sampling approaches to solving neural SDE models. While stochastic Runge–Kutta methods are typically either concerned with strong (pathwise) or weak (in distribution) solutions, we leverage the even weaker solution concept of only tracking the first two moments of the solution. This simplification of turning solving the SDE into a deterministic ODE problem of its moments, comes with some remarkable computational savings, and often suffice in practical modelling. Then again, the proposed method does not lend itself well to cases where pathwise sample trajectories are required.

We recognize that we cannot give guarantees for the approximated Gaussian integrals to capture the evolution of the true moments outside particular special cases (*e.g.*, 3rd order cubature is exact for polynomials up to order 3). Yet the performance on practical applications is considered reliable, and these kinds of approaches are commonly employed across assumed density filtering in signal processing. The use of the approximations schemes we present inherently makes the assumption that the time-marginals of the process are of higher interest compared to the pathwise solutions to the SDE. While the sampling-based methods are less efficient than assumed density approximations, their use is well-justified in applications where sampling trajectories is the purpose of the application.

Codes for the methods and experiments in this paper are available at <http://github.com/AaltoML/scalable-inference-in-SDEs>.

Acknowledgments and Disclosure of Funding

Authors acknowledge funding from Academy of Finland (grant numbers 324345 and 339730). We also wish to thank the anonymous reviewers for their comments on our manuscript, and Çağatay Yıldız and Xuechen Li for providing useful details on the MOCAP experiment. We acknowledge the computational resources provided by the Aalto Science-IT project. ET has been employed part-time at Sellforte Oy during the project. The MOCAP data was obtained from mocap.cs.cmu.edu (created with funding from NSF EIA-0196217).

References

- [1] CMU graphics lab motion capture database. URL <http://mocap.cs.cmu.edu/>.
- [2] J. Ala-Luhtala, S. Särkkä, and R. Piché. Gaussian filtering and variational approximations for Bayesian smoothing in continuous-discrete stochastic dynamic systems. *Signal Processing*, 111:124–136, 2015.
- [3] I. Arasaratnam and S. Haykin. Cubature Kalman filters. *IEEE Transactions on Automatic Control*, 54(6): 1254–1269, 2009.
- [4] C. Archambeau and M. Opper. Approximate inference for continuous-time Markov processes. In *Bayesian Time Series Models*, pages 125–140. Cambridge University Press, New York, NY, 2011.
- [5] F. P. Casale, A. V. Dalca, L. Saglietti, J. Listgarten, and N. Fusi. Gaussian process prior variational autoencoders. In *Advances in Neural Information Processing Systems 31 (NeurIPS)*, volume 31, pages 10369–10380. Curran Associates, Inc., 2018.

- [6] R. T. Q. Chen, Y. Rubanova, J. Bettencourt, and D. K. Duvenaud. Neural ordinary differential equations. In *Advances in Neural Information Processing Systems 31 (NeurIPS)*, pages 6571–6583. Curran Associates, Inc., 2018.
- [7] R. Cools. Constructing cubature formulae: The science behind the art. In *Acta Numerica*, volume 6, pages 1–54. 1997.
- [8] R. Frigola, Y. Chen, and C. E. Rasmussen. Variational Gaussian process state-space models. In *Advances in Neural Information Processing Systems 27 (NIPS)*, pages 3680–3688. Curran Associates, Inc., 2014.
- [9] Z. Gan, C. Li, R. Henao, D. E. Carlson, and L. Carin. Deep temporal sigmoid belief networks for sequence modeling. In *Advances in Neural Information Processing Systems 28 (NIPS)*, pages 2467–2475. Curran Associates, Inc., 2015.
- [10] A. Gelb, editor. *Applied Optimal Estimation*. MIT Press, Cambridge, MA, 1974.
- [11] W. Grathwohl, R. T. Q. Chen, J. Bettencourt, and D. Duvenaud. Scalable reversible generative models with free-form continuous dynamics. In *International Conference on Learning Representations (ICLR)*, 2019.
- [12] J.-S. Ha, Y.-J. Park, H.-J. Chae, S.-S. Park, and H.-L. Choi. Adaptive path-integral autoencoders: Representation learning and planning for dynamical systems. In *Advances in Neural Information Processing Systems 31 (NeurIPS)*, pages 8927–8938. Curran Associates, Inc., 2018.
- [13] P. Hegde, M. Heinonen, H. Lähdesmäki, and S. Kaski. Deep learning with differential Gaussian process flows. In *Proceedings of the 22nd International Conference on Artificial Intelligence and Statistics*, volume 89 of *Proceedings of Machine Learning Research*, pages 1812–1821. PMLR, 2019.
- [14] M. Heinonen, C. Yildiz, H. Mannerström, J. Intosalmi, and H. Lähdesmäki. Learning unknown ODE models with Gaussian processes. In *Proceedings of the 35th International Conference on Machine Learning*, volume 80 of *Proceedings of Machine Learning Research*, pages 1959–1968. PMLR, 2018.
- [15] J. Hensman, A. G. d. G. Matthews, and Z. Ghahramani. Scalable variational Gaussian process classification. In *Proceedings of the 18th International Conference on Artificial Intelligence and Statistics*, volume 28 of *Proceedings of Machine Learning Research*. PMLR, 2015.
- [16] J. Ho, A. Jain, and P. Abbeel. Denoising diffusion probabilistic models. In *Advances in Neural Information Processing Systems 33 (NeurIPS)*. Curran Associates, Inc., 2020.
- [17] A. H. Jazwinski. *Stochastic Processes and Filtering Theory*. Academic Press, New York, 1970.
- [18] P. Kidger, J. Morrill, J. Foster, and T. Lyons. Neural controlled differential equations for irregular time series. In *Advances in Neural Information Processing Systems 33 (NeurIPS)*. Curran Associates, Inc., 2020.
- [19] P. Kidger, J. Foster, X. Li, and T. J. Lyons. Neural sdes as infinite-dimensional gans. In *Proceedings of the 38th International Conference on Machine Learning*, volume 139 of *Proceedings of Machine Learning Research*, pages 5453–5463, 2021.
- [20] D. P. Kingma and J. Ba. Adam: A method for stochastic optimization. *arXiv preprint arXiv:1412.6980*, 2014.
- [21] D. P. Kingma and M. Welling. Auto-encoding variational Bayes. In *2nd International Conference on Learning Representations (ICLR)*, 2014.
- [22] P. E. Kloeden, E. Platen, and H. Schurz. *Numerical Solution of SDE Through Computer Experiments*. Springer Science & Business Media, 2012.
- [23] H. Kushner. Approximations to optimal nonlinear filters. *IEEE Transactions on Automatic Control*, 12(5): 546–556, 1967.
- [24] N. D. Lawrence and A. J. Moore. Hierarchical Gaussian process latent variable models. In *Proceedings of the 24th International Conference on Machine Learning*, Proceedings of Machine Learning Research, pages 481–488. PMLR, 2007.
- [25] Y. LeCun, C. Cortes, and C. J. Burges. The MNIST database of handwritten digits, 1998. URL <http://yann.lecun.com/exdb/mnist/>.
- [26] X. Li, T.-K. L. Wong, R. T. Q. Chen, and D. Duvenaud. Scalable gradients for stochastic differential equations. In *Proceedings of the 23rd International Conference on Artificial Intelligence and Statistics*, volume 108 of *Proceedings of Machine Learning Research*, pages 3870–3882. PMLR, 2020.

- [27] A. Look, C. Qiu, M. Rudolph, J. Peters, and M. Kandemir. Deterministic variational inference of neural SDEs. *arXiv preprint arXiv:2006.08973:v1*, 2020. NB: A moment matching/linearization approach is discussed only in the initial version (v1) of the manuscript.
- [28] A. G. d. G. Matthews, M. van der Wilk, T. Nickson, K. Fujii, A. Boukouvalas, P. León-Villagrà, Z. Ghahramani, and J. Hensman. GPflow: A Gaussian process library using TensorFlow. *Journal of Machine Learning Research*, 18(40):1–6, apr 2017.
- [29] P. S. Maybeck. *Stochastic Models, Estimation and Control*, volume 2. Academic Press, New York, NY, 1982.
- [30] B. Øksendal. *Stochastic Differential Equations: An Introduction with Applications*. Springer, New York, NY, sixth edition, 2003.
- [31] T. Ozaki. A bridge between nonlinear time series models and nonlinear stochastic dynamical systems: a local linearization approach. *Statistica Sinica*, 2(1):113–135, 1992.
- [32] A. Papoulis. *Probability, Random Variables, and Stochastic Processes*. McGraw-Hill, Singapore, 1984.
- [33] A. Paszke, S. Gross, F. Massa, A. Lerer, J. Bradbury, G. Chanan, T. Killeen, Z. Lin, N. Gimelshein, L. Antiga, A. Desmaison, A. Kopf, E. Yang, Z. DeVito, M. Raison, A. Tejani, S. Chilamkurthy, B. Steiner, L. Fang, J. Bai, and S. Chintala. PyTorch: An imperative style, high-performance deep learning library. In *Advances in Neural Information Processing Systems 32 (NeurIPS)*, pages 8024–8035. Curran Associates, Inc., 2019.
- [34] C. E. Rasmussen and C. K. I. Williams. *Gaussian Processes for Machine Learning*. MIT Press, 2006.
- [35] D. J. Rezende, S. Mohamed, and D. Wierstra. Stochastic backpropagation and approximate inference in deep generative models. In *Proceedings of the 31st International Conference on Machine Learning*, volume 32 of *Proceedings of Machine Learning Research*, pages 1278–1286. PMLR, 2014.
- [36] L. C. G. Rogers and D. Williams. *Diffusions, Markov Processes and Martingales, Volume 2: Itô Calculus*. Cambridge Mathematical Library. Cambridge University Press, Cambridge, 2000.
- [37] Y. Rubanova, R. T. Q. Chen, and D. K. Duvenaud. Latent ordinary differential equations for irregularly-sampled time series. In *Advances in Neural Information Processing Systems 32 (NeurIPS)*, pages 5320–5330. Curran Associates, Inc., 2019.
- [38] A. Ruttor, P. Batz, and M. Opper. Approximate Gaussian process inference for the drift function in stochastic differential equations. In *Advances in Neural Information Processing Systems 26 (NIPS)*, pages 2040–2048. Curran Associates, Inc., 2013.
- [39] S. Särkkä and J. Sarmavuori. Gaussian filtering and smoothing for continuous-discrete dynamic systems. *Signal Processing*, 93(2):500–510, 2013.
- [40] S. Särkkä and A. Solin. *Applied Stochastic Differential Equations*. Cambridge University Press, 2019.
- [41] I. Shoji and T. Ozaki. Estimation for nonlinear stochastic differential equations by a local linearization method. *Stochastic Analysis and Applications*, 16(4):733–752, 1998.
- [42] L. Socha. *Linearization Methods for Stochastic Dynamic Systems*, volume 730 of *Lecture Notes in Physics*. Springer, Berlin, 2008.
- [43] Y. Song and S. Ermon. Generative modeling by estimating gradients of the data distribution. In *Advances in Neural Information Processing Systems 32 (NeurIPS)*, pages 11918–11930. Curran Associates, Inc., 2019.
- [44] Y. Song, J. Sohl-Dickstein, D. P. Kingma, A. Kumar, S. Ermon, and B. Poole. Score-based generative modeling through stochastic differential equations. *arXiv preprint, arXiv:2011.13456*, 2020.
- [45] M. Titsias and N. D. Lawrence. Bayesian Gaussian process latent variable model. In *Proceedings of the 13th International Conference on Artificial Intelligence and Statistics*, volume 9 of *Proceedings of Machine Learning Research*, pages 844–851. PMLR, 2010.
- [46] B. Tzen and M. Raginsky. Neural stochastic differential equations: Deep latent Gaussian models in the diffusion limit. *arXiv preprint arXiv:1905.09883*, 2019.
- [47] N. Wahlström. *Modeling of Magnetic Fields and Extended Objects for Localization Applications*. PhD thesis, Linköping University, Sweden, 2015.

- [48] C. Yildiz, M. Heinonen, J. Intosalmi, H. Mannerstrom, and H. Lahdesmaki. Learning stochastic differential equations with Gaussian processes without gradient matching. In *2018 IEEE 28th International Workshop on Machine Learning for Signal Processing (MLSP)*, pages 1–6, 2018.
- [49] C. Yıldız, M. Heinonen, and H. Lahdesmaki. ODE²VAE: Deep generative second order ODEs with Bayesian neural networks. In *Advances in Neural Information Processing Systems 32 (NeurIPS)*, pages 13412–13421. Curran Associates, Inc., 2019.

Supplementary Material:

Scalable Inference in SDEs by Direct Matching of the Fokker–Planck–Kolmogorov Equation

This supplementary document is organized as follows. App. A provides further details and derivations to facilitate understanding of the methodology. App. B includes full details on the experiments, baseline methods, data sets, and additional results.

A Methodological Details

We provide details in terms of the concept of ‘solution’ to an SDE, how we use a finite-differences approach for solving the FPK as baseline, and comments on the existence properties of the GP-SDE model formulation.

A.1 On the Concept of a Solution of an SDEs

As illustrated in Fig. 1 in the main paper, the concept of a ‘solution’ to an SDE is broader than that of an ODE. We restrict our interest to Itô type SDEs, and consider two types of solution concepts here: (i) Strong (path-wise) solutions, and (ii) weak (in-distribution) solutions.

A strong solution trajectory $\hat{\mathbf{z}}(t)$ to an SDE resembles an ‘actual’ (ideal, often intractable in practice) solution trajectory. For simulation methods, their order of strong convergence γ (see, *e.g.*, p. 132 in [40]) can be characterized by looking at the expected error after $M = 1/\Delta t$ steps of length Δt , $E[|\mathbf{z}(t_M) - \hat{\mathbf{z}}(t_M)|] \leq K\Delta t^\gamma$ for some constant K . However, it is generally non-trivial to construct high strong order solution methods to SDEs due to the requirement of solving intractable iterated Itô integrals in the Itô–Taylor series expansion. The required step size Δt thus remains very small; for example, the Euler–Maruyama method converges with a strong order of $\gamma = 1/2$, which makes it tricky to choose a small-enough step size to ensure the trajectories to resemble an actual solution trajectory. In machine learning, we might be interested in path-wise solutions in the case of drawing an example solution trajectory from the method that follows the evolution of a particular realization of the random forces affecting the output.

However, during training and testing time, we are typically more interested in *aggregating* properties over multiple solution trajectories to either capture the *typical* behaviour of the model or quantify *uncertainties* induced by the random forces in the model. As the model is stochastic, the full solution entails a probability distribution, $p(\mathbf{z}, t)$, depending on time t and covering the space \mathbf{z} .

The typical approach for characterizing $p(\mathbf{z}, t)$ in machine learning applications has been through simulation (sampling), where the Euler–Maruyama scheme, the Milstein scheme, or some more general stochastic Runge–Kutta scheme is often used. For simulation methods, the weak order of convergence (see, *e.g.*, p. 137 in [40]) can be used for characterizing the method, where it is defined to be the largest exponent α such that $|E[g(\mathbf{z}(t_M))] - E[g(\hat{\mathbf{z}}(t_M))]| \leq K\Delta t^\alpha$ for any polynomial function $g(\cdot)$. This is a much weaker criterion as it only considers the error in the expectation, and for example, the Euler–Maruyama method converges with weak order convergence $\alpha = 1$. In practice, this means that the moment properties can be captured with a more moderate step-size than the path-wise resemblance of the solutions.

However, if one is only interested in the first moments and/or if the dimensionality of \mathbf{z} is high, it makes sense to consider an even weaker solution concept, where one is only concerned with the first two moments of $p(\mathbf{z}, t) \approx N(\mathbf{m}(t), \mathbf{P}(t))$. This is what is done in this paper.

In short, capturing the true pathwise behaviour of an SDE is challenging (NB: simulation schemes do not generally capture this well) and sampling schemes instead generally capture the distribution by a finite set of samples. If you are interested in the first moments only, it can be generally safer to model those directly.

A.2 Approximating the FPK Solution Through Finite-differences

As a baseline in Fig. 4 we seek to seek direct ways of assessing the behaviour of the solution to the Fokker–Planck–Kolmogorov PDE or its transition density. For this we could use any tools from the vast literature of partial differential equation approximations. The approach presented here essentially uses finite differences in the input domain of \mathbf{z} and then solves the resulting homogeneous ODE system directly.

The Fokker–Planck–Kolmogorov equation has the form

$$\frac{\partial p(\mathbf{z}, t)}{\partial t} = \mathcal{A}^* p(\mathbf{z}, t), \quad (18)$$

where \mathcal{A}^* is the operator defined in Eq. (7) in the main paper. We can approximate this equation as a finite-dimensional system, which is a homogeneous linear system. We discretize the state space to a finite grid $\{(z_1^{(i)}, z_2^{(j)}) : i, j = 1, 2, \dots, N\}$ and then approximate the derivatives as finite differences. The approximations can, for example, be given by

$$\begin{aligned} \frac{\partial p(\mathbf{z}, t)}{\partial z_1} &\approx \frac{p(z_1 + \Delta z_1, z_2, t) - p(z_1 - \Delta z_1, z_2, t)}{2\Delta z_1}, \\ \frac{\partial^2 p(\mathbf{z}, t)}{\partial z_1^2} &\approx \frac{p(z_1 + \Delta z_1, z_2, t) - 2p(\mathbf{z}, t) + p(z_1 - \Delta z_1, z_2, t)}{\Delta z_1^2}, \end{aligned} \quad (19)$$

and analogously in the other dimension. We can now interpret Eq. (7) through these finite difference approximations and form a (very) sparse matrix corresponding to the adjoint operator \mathcal{A}^* , where also the drift and diffusion terms are evaluated at the discrete values. Thus the FPK can be rewritten as a linear ODE system

$$\frac{d\mathbf{p}}{dt} = \mathbf{A} \mathbf{p}, \quad (20)$$

where \mathbf{A} is the finite-difference approximation matrix for the operator \mathcal{A}^* . The initial conditions $p(\mathbf{z}, t_0)$ can also be collected into a vector $\mathbf{p}(t_0)$. Because our GP-SDE model is time-invariant, the solution to the homogeneous ODE initial value problem is directly given (in closed-form) as

$$\mathbf{p}(t) = \exp((t - t_0) \mathbf{A}) \mathbf{p}(t_0). \quad (21)$$

To better explain how this works in practice we have added a Jupyter notebook to this supplement which reproduces this approach.

A.3 On the GP-SDE Model Construction

The model which we call a ‘GP-SDE’ model in the main paper has appeared in various forms in literature before. It directly resembles a ‘random’ ODE model, where the random field $\mathbf{v}_\theta(\cdot)$ has previously typically either been characterized by a Gaussian random field or Gaussian process model (see, *e.g.*, [38, 13]) or some parametric model (*e.g.*, [26]). Yet, the existence of the corresponding SDE model as in Eqs. (4) and (5) is non-trivial.

The GP-SDE model is presented informally in the main paper, and we *do not* guarantee the existence of strong unique solutions to the corresponding SDE model. However, under GP increments, the weak solution of this model exists—which can also be directly empirically shown, *e.g.*, by sampling the GP in an Euler fashion vs. running Euler–Maruyama on the corresponding SDE. This highlights the *practical* aspects of this model, which is probably also why it has been appearing in various previous forms in machine learning literature.

B Experiment Details

We provide additional details and results for the experiments presented in the paper, and further evaluate the computational costs of linearized approximation. Fig. 10 follows the same structure as Fig. 6 in the main paper, just providing further examples from the test set.

B.1 Empirical Wall-Clock Timing Experiments

For the timing experiments in Sec. 3, we constructed a setup that allowed us to control the approximation error. We used the Beneš SDEs model (see details on this, *e.g.*, in [40]) that has the form

$$dz(t) = \tanh(z(t)) dt + d\beta(t), \quad (22)$$

where $\beta(t)$ is standard Brownian motion and the initial state z_0 is known. This model is non-linear in the drift and the solution is not directly apparent. Conveniently, this model has a closed-form solution that we can leverage as a control. The transition density or solution to the FPK equation is given as:

$$p(z, t) = \frac{1}{\sqrt{2\pi t}} \frac{\cosh(z)}{\cosh(z_0)} \exp\left(-\frac{1}{2}t\right) \exp\left(-\frac{1}{2t}(z - z_0)^2\right). \quad (23)$$

This solution is bi-modal and thus the moment matching approach will be an approximation to the true solution distribution. Also the first two moments are available in closed-form and given by:

$$\begin{aligned} m(t) &= z_0 + \tanh(z_0) t, \\ P(t) &= z_0^2 + 2z_0 \tanh(z_0) t + t + t^2 - [m(t)]^2. \end{aligned} \quad (24)$$

This model is one-dimensional in z , but we expand it to $\mathbf{z} \in \mathbb{R}^d$ by considering d independent Beneš SDE models over \mathbf{z} with different $z_0^{(d)}$. The initial points of the trajectories were chosen with linear spacing in $[0, 1]$, with a step size of $1/d$. This test setup should be favourable to a stochastic Runge–Kutta approach, where the samples now do not need to account for correlation in the latent space, thus pushing down the required number of sample trajectories, which we expect to be linear in d (the assumption of a diagonal diffusion was encoded in the experiment setup *a priori*, and the independence of the dimensions in the diffusion function was not). We thus claim that this experiment rather highlights the worst case benefits of our method, rather than the best case.

The number of trajectories used in the stochastic Euler–Mauryama was chosen to match the KL divergence of the moment matching approximation. That is, we initially completed the moment matching approximation for a given dimensionality d , obtaining the moments $\mathbf{m}_{\text{mm}}(t)$, $\mathbf{P}_{\text{mm}}(t)$, which were compared to the closed-form moments in Eq. (24) by the Kullback–Leibler distance. We evaluated the KL divergence at one hundred values of t (with a spacing of 0.1), and calculated the total divergence as a sum of the divergence at individual points.

In order to determine the number of trajectories generating moments of a comparable quality to the moment matching approach, we computed the first two moments over a varying number of trajectories. The moments were compared to the true Beneš SDE moments with the same KL divergence metric as the moment approximation. For each d , we matched the number of trajectories n by controlling that

$$D_{\text{KL}} \left[\mathcal{N}(\mathbf{m}_{\text{EM}}^{(n)}(t), \mathbf{P}_{\text{EM}}^{(n)}(t)) \parallel \mathcal{N}(\mathbf{m}(t), \mathbf{P}(t)) \right] \leq D_{\text{KL}} \left[\mathcal{N}(\mathbf{m}_{\text{mm}}(t), \mathbf{P}_{\text{mm}}(t)) \parallel \mathcal{N}(\mathbf{m}(t), \mathbf{P}(t)) \right], \quad (25)$$

where $(\mathbf{m}(t), \mathbf{P}(t))$ are the exact moments, $(\mathbf{m}_{\text{EM}}^{(n)}(t), \mathbf{P}_{\text{EM}}^{(n)}(t))$ the moments from the Euler–Mauryama solution with n trajectories, and $(\mathbf{m}_{\text{mm}}(t), \mathbf{P}_{\text{mm}}(t))$ the moments from our moment matching approach. As sampling methods are stochastic, we generated n trajectories 10 times, to account for the uncertainty. For low values of d , the standard deviation of the KL divergence was in the range of 10–20% of the mean value, whereas for higher values of d , such as 200 or 500, the uncertainty of the metric was reduced to at most a percentage of the mean.

For this experiment, where the dimensions are uncorrelated, we found that the required number of trajectories to obtain the KL divergence of moment matching approximations was, depending on the dimensionality, between $1d$ and $2d$ (for dimensions [10, 50, 200, 300, 400, 500], the number of trajectories in the same order was [25, 65, 225, 325, 440, 550]). While the linearized approximation generally was less accurate than moment matching, it was equivalent to a nearly as high number of trajectories as moment matching (for example, when $d = 200$, linearized approximation was comparable to 210 trajectories, and moment matching to 225 trajectories).

We implement the models in PyTorch [33] and report means of 10 repetitions (std over runs negligible and omitted for clarity of presentation). The GPU/CPU wall-clock times that are reported in the main paper were run on a cluster with separate GPU and CPU partitions (GPU: NVIDIA Tesla V100 32 GB with Intel Xeon Gold 6134 3.2 GHz; CPU: Xeon Gold 6248 2.50 GHz).

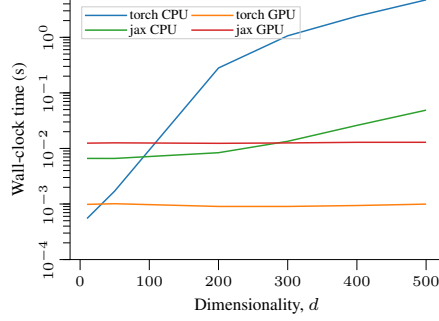


Figure 7: Empirical timing experiments of Jacobian evaluations over a single point. The variation between repetitions was negligible, and is omitted for clarity.

B.2 Additional Jacobian Computation Timing Experiment

As we note in Sec. 2.6, a single step of linearized approximation requires only $\mathcal{O}(1)$ drift, diffusion and Jacobian evaluations. When the drift function is defined by a neural network, the scaling of the computational costs from evaluating the Jacobian is not inherently clear, as the network size is grown. In order to better assess the empirical computational costs of linearized approximation in dimension d , we evaluate the Jacobian of a neural network with two hidden layers, each with $3d$ nodes. The experiment results presented in Fig. 7 demonstrate that when GPU resources are available, the cost of evaluating the Jacobian in linearized approximation is not a bottleneck for growing the network size or approximating SDEs in high-dimensional spaces. The experiment set-up in terms of hardware used is as in App. B.1, and the Jacobian was evaluated 10 times, the first of which was discarded due to initialization overhead.

B.3 GP-SDE Model Specification

This example was included to highlight the idea behind the GP-SDE model in a simple task, where encoding prior knowledge plays a major role in the outcome. We considered a GP-SDE model with just 8 observations of the dynamics, where the lack of data can be compensated for by encoding prior knowledge into the model. We use the model formulation given in Sec. 2.1, and study the effect of GP priors, the first of which is an independent squared exponential (RBF) prior for each dimension which encodes continuity and smoothness in the velocity field. The second GP prior is the multi-dimensional curl-free kernel [47]:

$$\kappa_{\text{cf}}(\mathbf{z}, \mathbf{z}') = \frac{\sigma^2}{\ell^2} e^{-\frac{\|\mathbf{z}-\mathbf{z}'\|^2}{2\ell^2}} \left[\mathbf{I} - \left(\frac{\mathbf{z}-\mathbf{z}'}{\ell} \right) \left(\frac{\mathbf{z}-\mathbf{z}'}{\ell} \right)^\top \right], \quad (26)$$

which encodes the assumption of a curl-free random vector field. This property can be interpreted as ‘loop aversion’ in the GP-SDE context. The third prior, is a multi-dimensional divergence-free kernel [47]:

$$\kappa_{\text{df}}(\mathbf{z}, \mathbf{z}') = \frac{\sigma^2}{\ell^2} e^{-\frac{\|\mathbf{z}-\mathbf{z}'\|^2}{2\ell^2}} \left[\left(\frac{\mathbf{z}-\mathbf{z}'}{\ell} \right) \left(\frac{\mathbf{z}-\mathbf{z}'}{\ell} \right)^\top + \left((d-1) - \frac{\|\mathbf{z}-\mathbf{z}'\|^2}{\ell^2} \right) \mathbf{I} \right], \quad (27)$$

which encodes the assumption of no divergence in the random vector field. This property can be interpreted as ‘energy preservation’ or source-freeness. These properties are visible in Fig. 3, where the hyperparameters are fixed to same values for all models (even if the interpretation differs).

B.4 Synthetic Race Track

As an additional example, we run the proposed algorithm on two synthetic race-tracks: oval-shaped and bean-shaped. For both the experiments, we have a true race track and a set of noisy observed race tracks. The latent state, $\mathbf{z} \in \mathbb{R}^2$, governs the dynamics in the original space. Further, using the noisy observed race tracks, we create a set of observation vectors on which the GP is conditioned. For this, we use the Gaussian process regression model in the GPflow [28] framework with the

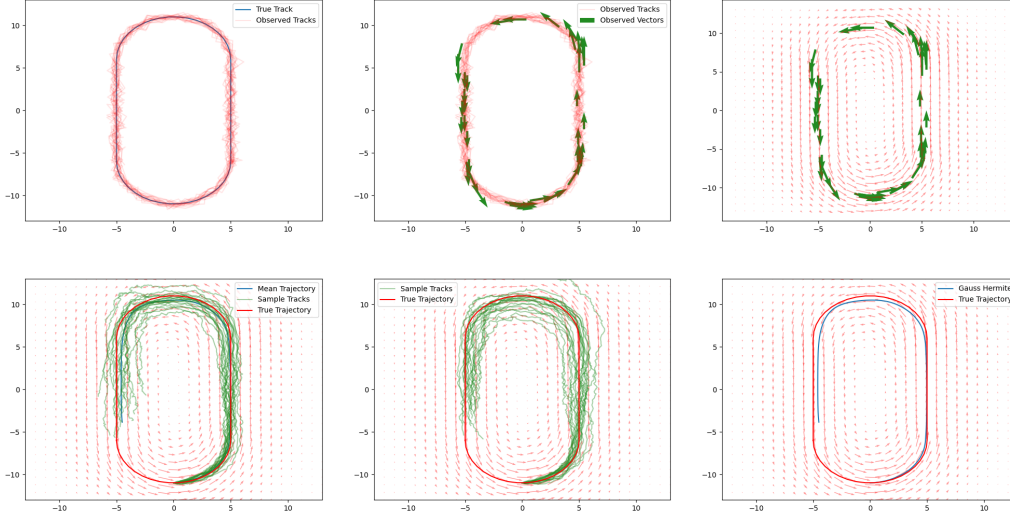


Figure 8: The output of oval shaped synthetic car race track. (a) True track and noisy observation tracks. (b) Observation vectors and observation tracks. (c) Mean predicted vector field of the GP-SDE. (d) Trajectories predicted using the Euler scheme for the ‘random ODE’ interpretation, with dynamics drawn from GP samples. (e) Trajectories predicted by the Euler–Maruyama scheme for the GP-SDE model. (f) Mean trajectory path predicted using Gauss–Hermite quadrature by assumed density.

squared-exponential (RBF) kernel. The hyperparameters of the model are optimized with the Adam optimizer with a learning rate of 0.001, and the kernel hyperparameters are initialized with default values, length-scale and variance 1.0.

Fig. 8 and Fig. 9 showcase the outputs on the two synthetic race tracks. The figures show the true track and noisy observations of the dynamics along the trajectory. On top-right, the mean predicted vector field of the GP-SDE for these observations. Then we visually compare trajectories predicted using the Euler scheme for the ‘random ODE’ interpretation, where the dynamics are drawn from GP samples (see Eq. (1) in the main paper), with trajectories predicted by the Euler–Maruyama scheme for the GP-SDE model. Finally, we plot the mean trajectory path predicted using 4th order Gauss–Hermite quadrature by an assumed density assumption.

B.5 Rotating MNIST

In the spirit of Fig. 2, we run the proposed methods on Rotating MNIST ([25], available under CC BY-SA 3.0), similar to [49, 5]. The data set consists of various handwritten digit ‘3’s rotated uniformly in 64 angles. The training data set is generated by randomly selecting 180 different versions of digit ‘3’ resulting in the total size of the training data set to be 11,520 images. A separate set of 20 digits are chosen to form a test set. We train a VAE [21] first by freezing the latent space dynamics, and then freezing the VAE encoder/decoder and training a 16-dimensional GP-SDE model in the latent space with independent squared exponential GP priors (see App. B.5). We implement the VAE model in PyTorch [33] and use GPflow [28] for the latent GP model. The latent space is chosen to be $d = 16$ dimensional and a sparse variational Gaussian process (SVGP) model [15] with 1000 trainable inducing points is leveraged to scale the GP training. We use independent squared-exponential prior covariance function for each latent dimension dynamics. The models are trained with the Adam optimizer [20] (learning rate 0.001), and the VAE loss function is a weighted sum of binary cross-entropy and KL-divergence, whereas the GP objective function is the ELBO. The training of the two components is disjoint, and the GP is trained on a fixed latent space given by a trained VAE.

An output of a test point is illustrated in Fig. 6, where we feed in one observation and let it follow the learned dynamics of rotation. As the baseline, we use 1000 trajectories computed using Euler–Maruyama with step length 0.1. Fig. 6a demonstrates the model’s capability to learn the latent trajectory, and we show the trajectories for all the methods in three latent dimensions with the

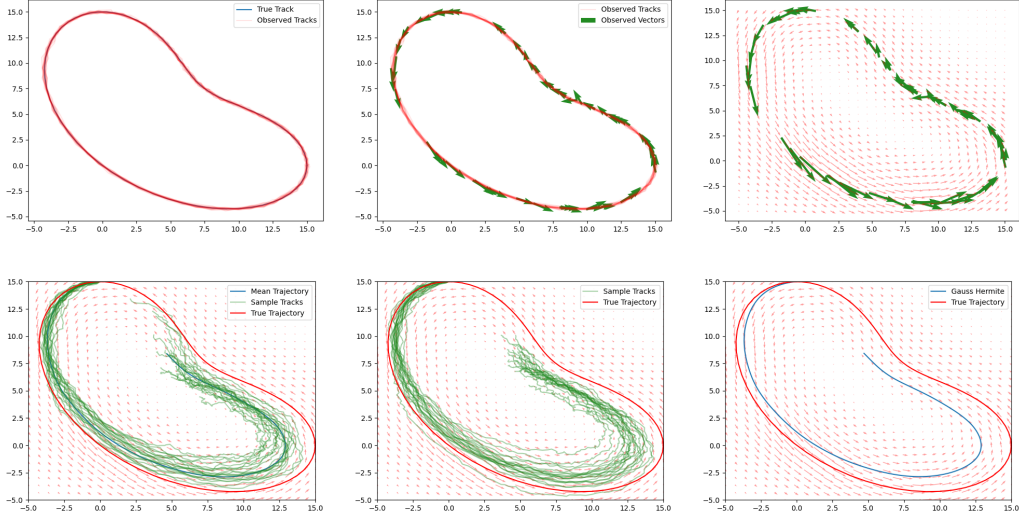


Figure 9: The output of bean shaped synthetic car race track. (a) True track and noisy observation tracks. (b) Observation vectors and observation tracks. (c) Mean predicted vector field of the GP-SDE. (d) Trajectories predicted using the Euler scheme for the ‘random ODE’ interpretation, with dynamics drawn from GP samples. (e) Trajectories predicted by the Euler–Maruyama scheme for the GP-SDE model. (f) Mean trajectory path predicted using Gauss–Hermite quadrature by assumed density.

most variation. The trajectories for the three methods overlap exactly, which also shows in Fig. 6b that shows the generated outputs in the observation space together with the associated marginal uncertainties. We include further details in Fig. 10.

For quantitative comparison, we do a 10-fold cross-validation study on the rotating MNIST data. The full dataset consists of 200 randomly chosen digits ‘3’ which are split into 10 folds, each fold consisting of 180 training and 20 test digits. As discussed, each digit is uniformly rotated around 64 angles thus making the training dataset size equal to 11,520. Both the models, VAE and latent-GP, are trained independently with the same initial hyperparameter values and an equal number of epochs over different folds. On the test dataset, we perform inference via three schemes: Euler–Maruyama, linearization, and moment matching. Euler–Maruyama acts as a baseline for which 1000 samples with 0.1 step-size are generated. For linearization and moment-matching we use the Euler scheme with 0.1 step-size for solving the resulting ODE. The MSE values are calculated for the mean. Alongside mean we also characterize the uncertainty estimates by studying the negative log probability density (NLPD) for all the three schemes in the latent space over time. The MSE and (final-step, $t = 64$) NLPD results are in Table 1 in the main paper, where we see that the sampling scheme performs slightly better, especially in terms of NLPD—even if the qualitative results did not show a clear difference.

B.6 Motion Capture Experiment Details

For the motion capture experiments, we used the same pre-processed CMU Walking data set as in Yıldız et al. [49]. The relevant hyperparameters and design choices were the weighting of KL-divergence, learning rate of the optimizer, neural network designs, choice of SDE approximation, choice of the ODE solver, and choice of the prior process for regularization.

For weighting the KL-divergence, we tested the values $\gamma = \{1.0, 0.1\}$, both with a linear schedule until epoch 200 and fixed value. The listed MSE was achieved when using $\gamma = 1$ fixed and with a learning rate of 0.01. The drift, diffusion, encoder and decoder networks were all trained simultaneously in 1500 iterations using the Adam optimizer, see Fig. 11 for the detailed network designs. With the exception that we model the change in the latent context, the neural networks are similar to those presented in Li et al. [26].

For the prior process, we used a simple stochastic process with zero drift and $0.1\mathbf{I}$ diffusion. In our experiments, we found that using a prior process is fundamental for successful training over an SDE

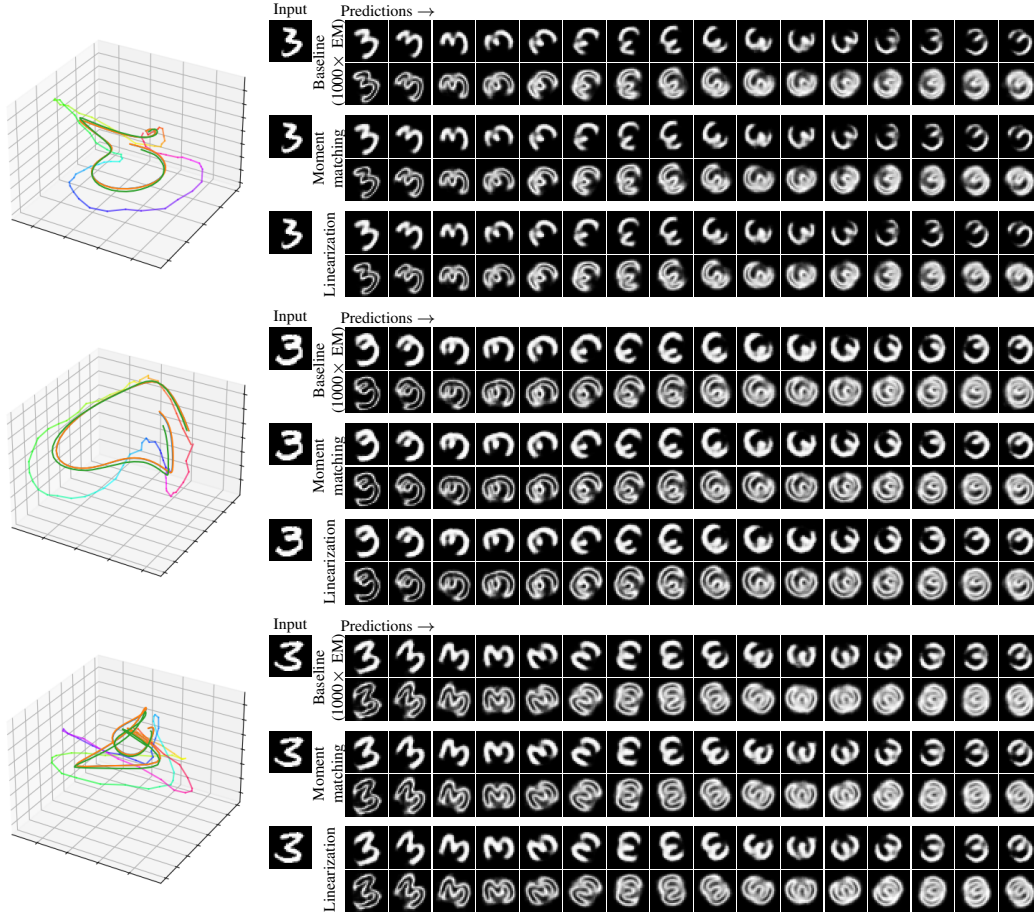


Figure 10: Further test set example results on the rotating MNIST data set. The left-hand side shows the prediction trajectories for one test set image in the latent space. Evolution of the true trajectory is shown in HSV colour code and the predicted trajectory by Euler–Maruyama, moment matching, and linearization scheme is shown in green, blue, and orange, respectively (all overlapping one another). The right-hand figures show the progression of the prediction (mean and marginal std images) of the test set image input, when it traverses the learned dynamics in the latent space. Both the moment matching and linearization schemes match the baseline (computed with 1000 Euler–Maruyama trajectories).

approximation: optimizing solely for maximum likelihood resulted in unrealistic parameter values and lead to numerical instability. As an alternative to zero drift prior processes, we tested a trainable drift network, and inspired by Li et al. [26], a prior diffusion network that matches the posterior in state dimensions. While the alternative prior processes produced a more informative latent space, we chose the zero drift prior process both for its simplicity and performance: the lowest MSE was achieved when using a zero drift prior. The selected ODE solver was a 5th order Runge–Kutta method. When running the model implementation for a linearized approximation on TensorFlow and a Tesla V100 GPU, training was completed in approximately 2 hours and 45 minutes.

We also include a separate timing comparison between the methods under this model, where we control for equal step size and between methods and using the plan Euler/Euler–Maruyama scheme. The results in Table 2 show timings for one pass with a PyTorch implementation and using the same hardware as presented in App. B.1.

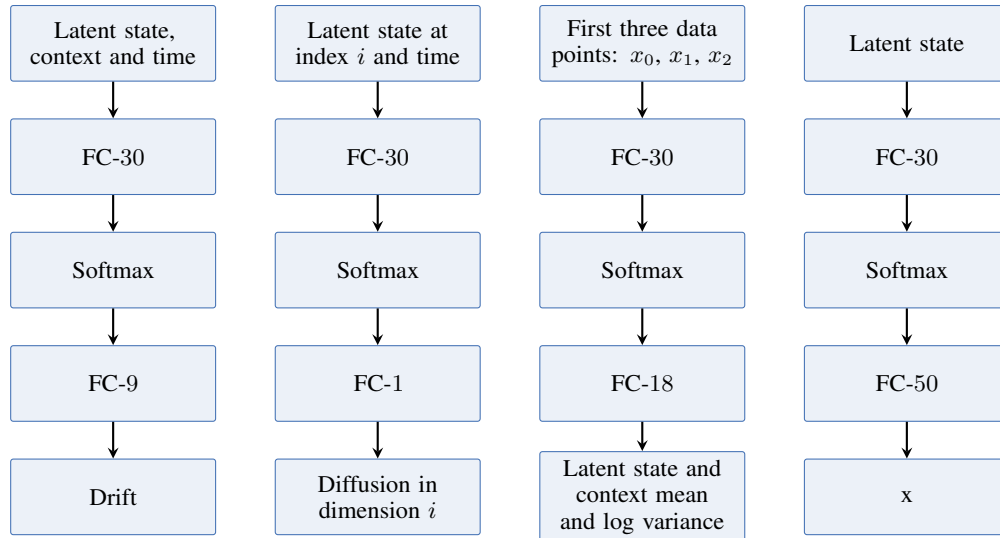


Figure 11: Neural network designs (from left to right) for the drift, diffusion, encoder and decoder networks. The diffusion network is duplicated 9 times, one for each latent state or context dimension.

C Author Contributions

The original idea and motivation for this work was conceived by AS, who also wrote a first draft of the paper. ET had the main responsibility of writing the related work section, the computational complexity section, and the MOCAP experiment. PV worked on the GP-SDE models and had the main responsibility of the rotating MNIST experiment. All authors contributed to finalizing the manuscript.